Chapter 13
Photonic Transition in Nanophotonics

Zongfu Yu and Shanhui Fan

13.1 Introduction

Photonic transition [1] is induced by refractive index modulation. Many photonic structures, including photonic crystals, or waveguides, can be described by a photonic band structure. When these structures are subject to temporal refractive index modulation, photon states can go through interband transitions, in a direct analogy to electronic transitions in semiconductors. Such photonic transitions have been recently demonstrated experimentally in silicon microring resonators [2]. In this chapter, we review two applications using the photonic transitions.

As the first application, we show that based on the effects of photonic transitions, a linear, broadband, and nonreciprocal isolator [3] can be accomplished by spatial–temporal refractive index modulations that simultaneously impart frequency and wavevector shifts during the photonic transition process. This work demonstrates that on-chip isolation can be accomplished with dynamic photonic structures, in standard material systems that are widely used for integrated optoelectronic applications.

In the second application, we show that a high-Q optical resonance can be created dynamically, by inducing a photonic transition between a localized state and a one-dimensional continuum through refractive index modulation [4]. In this mechanism, both the frequency and the external linewidth of a single resonance are specified by the dynamics, allowing complete control of the resonance properties.

This chapter is organized as follows: in Sect. 13.2, we review photonic transition induced by dynamic modulation; in Sects. 13.3 and 13.4, we describe the optical isolator and tunable cavity based on photonic transition, respectively; Sect. 13.5 is the conclusion part.

Z. Yu • S. Fan (✉)
Department of Electrical Engineering, Ginzton Laboratory, Stanford University,
350 Serra Mall (Mail Code: 9505), Stanford, CA 94305-9505, USA
e-mail: shanhui@stanford.edu

13.2   Photonic Transition in a Waveguide

We start by describing the photonic transition process in a silicon waveguide. The waveguide (assumed to be two-dimensional for simplicity) is represented by a dielectric distribution $\varepsilon_s(x)$ that is time-independent and uniform along the z-direction (Fig. 13.1b). Such a waveguide possesses a band structure as shown in Fig. 13.1a, with symmetric and antisymmetric modes located in the first and second band, respectively. An interband transition, between two modes with frequencies and wavevectors $(\omega_1, k_1), (\omega_2, k_2)$ located in these two bands, can be induced by modulating the waveguide with an additional dielectric perturbation:

$$\varepsilon'(x, z, t) = \delta(x) \, \cos(\Omega t - qz), \tag{13.1}$$

where $\delta(x)$ is the modulation amplitude distribution along the direction transverse to the waveguide. $\Omega = \omega_2 - \omega_1$ is the modulation frequency. Figure 13.1c shows
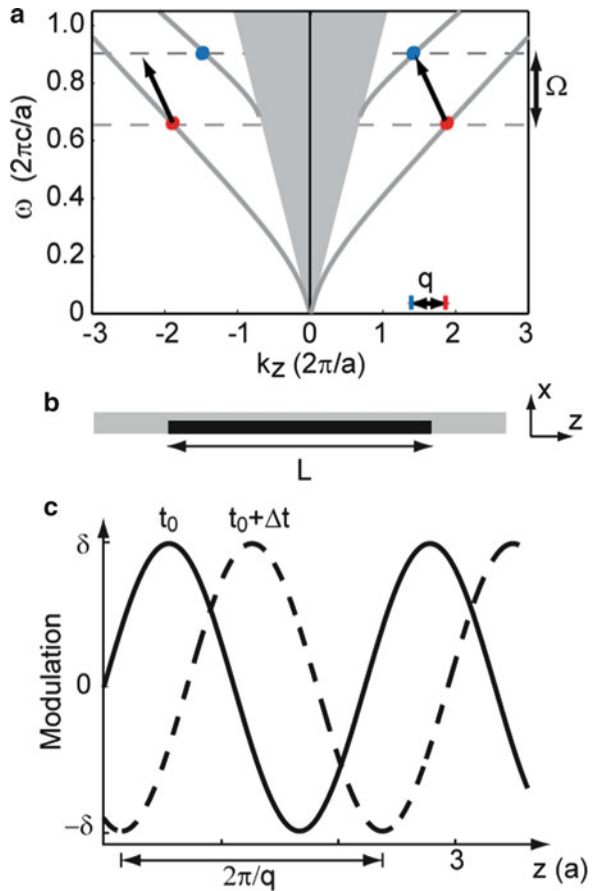

Fig. 13.1 (a) Band structure of a slab waveguide. (b) Structure of a silicon ($\varepsilon_s = 12.25$) waveguide. Modulation is applied to the dark region. (c) The modulation profile at two sequential time steps

the profile of the modulation. Such a transition, with $k_1 \neq k_2$, is referred to as an indirect photonic transition, in analogy with indirect electronic transitions in semiconductors.

We assume that the wavevector q approximately satisfies the phase-matching condition, i.e., $\Delta k = k_2 - k_1 - q \approx 0$. In the modulated waveguide, the electric field becomes:

$$E(x, z, t) = a_1(z)E_1(x)e^{i(-k_1 z + \omega_1 t)} + a_2(z)E_2(x)e^{i(-k_2 z + \omega_2 t)}, \qquad (13.2)$$

where $E_{1,2}(x)$ are the modal profiles, satisfying the orthogonal condition: (for simplicity, we have assumed the TE modes where the electric field has components only along the y-direction)

$$\frac{v_{gi}}{2\omega_i} \int_{-\infty}^{\infty} \varepsilon(x)E_i^* E_j = \delta_{ij}. \qquad (13.3)$$

In (13.3), the normalization is chosen such that $|a_n|^2$ is the photon number flux carried by the nth mode. By substituting (13.2) into the Maxwell's equations, and using slowly varying envelope approximation, we can derive the coupled mode equation:

$$\frac{d}{dz}\begin{pmatrix} a_1 \\ a_2 \end{pmatrix} = \begin{pmatrix} 0 & i\frac{\pi}{2l_c}\exp(-i\Delta kz) \\ i\frac{\pi}{2l_c}\exp(i\Delta kz) & 0 \end{pmatrix}\begin{pmatrix} a_1 \\ a_2 \end{pmatrix}, \qquad (13.4)$$

where

$$l_c = \frac{4\pi}{\varepsilon_0 \int\limits_{-\infty}^{\infty} \delta(x)E_1(x)E_2(x)dx}, \qquad (13.5)$$

is the coherence length. With an initial condition $a_1(0) = 1$ and $a_2(0) = 0$, the solution to (13.4) is:

$$a_1(z) = e^{-iz\Delta k/2}\left[\cos\left(\frac{z}{2l_c}\sqrt{\pi^2 + (l_c\Delta k)^2}\right)\right.$$

$$\left. +i\frac{l_c\Delta k}{\sqrt{\pi^2 + (l_c\Delta k)^2}}\sin\left(\frac{z}{2l_c}\sqrt{\pi^2 + (l_c\Delta k)^2}\right)\right] \qquad . \qquad (13.6)$$

$$a_2(z) = ie^{iz\Delta k/2}\frac{\pi}{\sqrt{\pi^2 + (l_c\Delta k)^2}}\sin\left(\frac{z}{2l_c}\sqrt{\pi^2 + (l_c\Delta k)^2}\right)$$

In the case of perfect phase-matching, i.e., $\Delta k = 0$, a photon initially in mode 1 will make a complete transition to mode 2 after propagating over a distance of coherence length l_c (Fig. 13.2a). In contrast, in the case of strong phase-mismatch, i.e., $l_c\Delta k \gg 1$, the transition amplitude is negligible (Fig. 13.2b).

Fig. 13.2 (**a**) Spatial
evolution of the photon
number flux of two modes
(*dashed line* mode 1 and *solid
line* mode 2), when a phase-
matching modulation is
applied to the waveguide.
(**b**) Maximum photon flux in
mode 2 as a function of phase
mismatch. The transition
becomes essentially
negligible at $l_c \Delta k \gg 1$
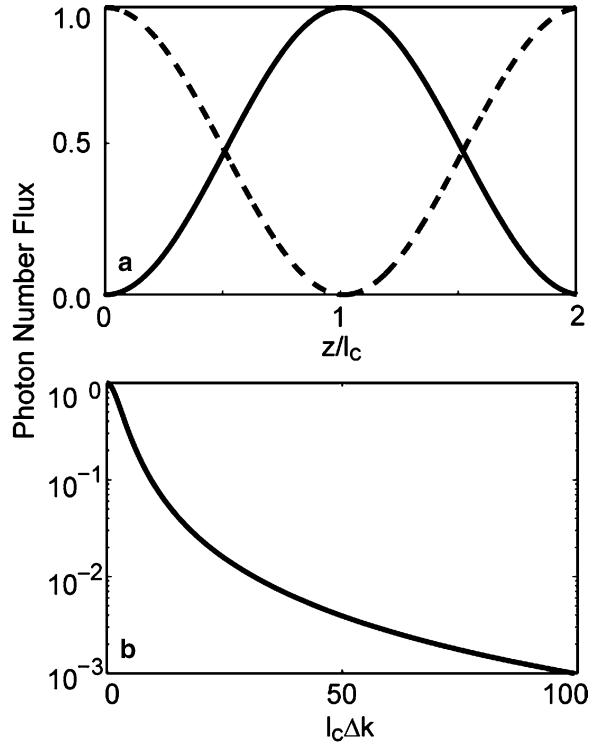
13.3   Photonic Transition for Integrated Optical Isolator

In this section, we use the photonic transition described in the previous section to
achieve on-chip optical isolation. In an optical network, isolators are an essential
component used to suppress back-reflection, and hence interference between dif-
ferent devices. Achieving on-chip optical signal isolation has been a fundamental
difficulty in integrated photonics. The need to overcome this difficulty, moreover,
is becoming increasingly urgent, especially with the emergence of silicon
nanophotonics, which promises to create on-chip optical systems at an unprece-
dented scale of integration.

   To create complete optical signal isolation requires simultaneous breaking of
both the time-reversal and the spatial inversion symmetry. In bulk optics, this is
achieved using materials exhibiting magneto-optical effects. Despite many efforts
[5–8], however, on-chip integration of magneto-optical materials, especially in
silicon in a CMOS compatible fashion, remains a great difficulty. Alternatively,
optical isolation has also been observed using nonlinear optical processes [9, 10], or
in electroabsorption modulators [11]. In either case, however, optical isolation
occurs only at specific power ranges, or with associated modulation side bands.
In addition, there have been works aiming to achieve partial optical isolation in
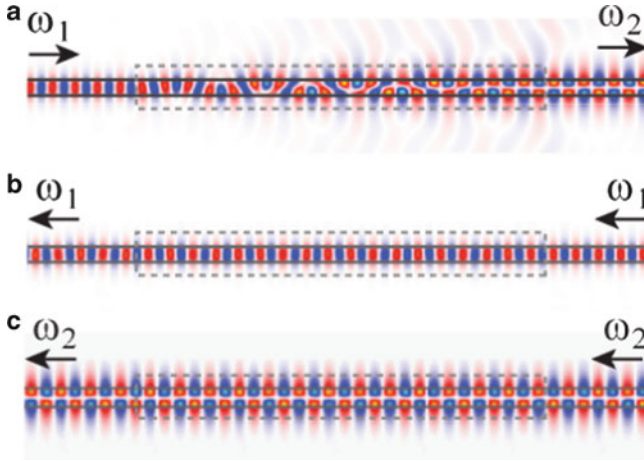
Fig. 13.3 Finite-difference time-domain simulation of an isolator based on photonic transitions. The *box* indicates the regions where the refractive index is modulated. *Blue/red* shows the amplitude of electric fields. *Arrows* indicate propagation directions

reciprocal structures that have no inversion symmetry (for example, chiral structures) [12]. In these systems, the apparent isolation occurs by restricting the allowed photon states in the backward direction, and would not work for arbitrary backward incoming states. None of the above nonmagnetic schemes can provide complete optical isolation.

In this part, we review and expand upon our recent works [3, 13] on creating complete and linear optical isolation using photonic transition. In these works, the temporal profile of the modulation used to induce the transition is chosen to break the time-reversal symmetry, while the spatial profile of the modulation is chosen to break the spatial-inversion and the mirror symmetry. As seen by the finite-difference time-domain simulations, when a silicon waveguide is under a modulation that induces an interband photonic transition, light of frequency ω_1 in forward direction is converted to a higher frequency mode ω_2 by the modulation (Fig. 13.3a). At the same time, light of frequencies ω_1 or ω_2 in the backward direction are not affected by the modulation (Fig. 13.3b, c). Combined with an absorption filter centered at ω_2, this structure can absorb all lights incident from one direction at ω_1, while passing those in the opposite direction, and thus creates a complete isolator behavior. It was also shown that the finite-difference time-domain simulations can also be well reproduced by coupled-mode theory [3].

We use the coupled mode theory as described in Sect. 13.2 to discuss the performance and design considerations for our dynamic isolator schemes. The waveguide system in Sect. 13.2 exhibits strong nonreciprocal behavior: the modulation in (13.1) does not phase-match the mode at $(\omega_1, -k_1)$ with any other mode of the system (Fig. 13.1a). Thus, while the mode at (ω_1, k_1) undergoes a complete photonic transition, its time-reversed counterpart at $(\omega_1, -k_1)$ is not affected at all. Such nonreciprocity arises from the breaking of *both* time-reversal

Fig. 13.4 Forward and
backward transmission
spectra without (**a**) and
with (**b**) modulation loss
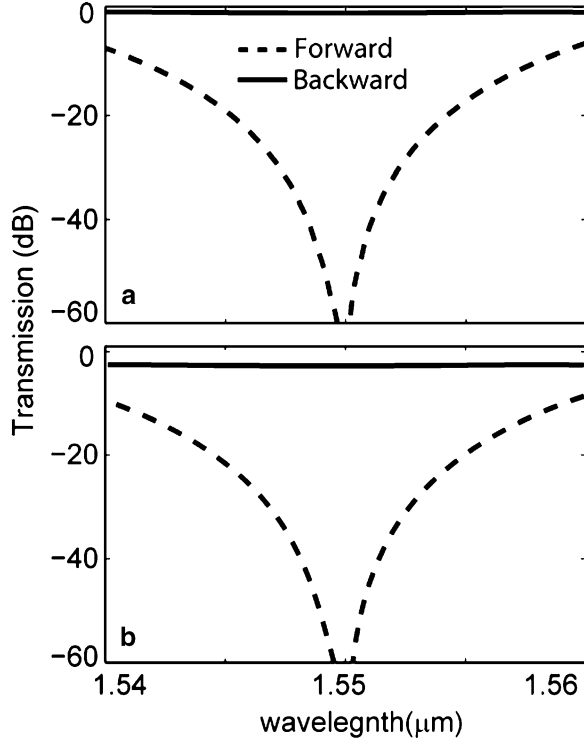
and spatial-inversion symmetries in the dynamics: The modulation in (13.1) is *not* invariant with either $t \rightarrow -t$ or $z \rightarrow -z$.

As a specific example, we consider a silicon ($\varepsilon = 12.25$) waveguide of 0.27 μm wide, chosen such that the first and second bands of the waveguide have the same group velocity around wavelength 1.55 μm (or a frequency of 193 THz). The modulation has a strength $\delta_{max}/\varepsilon_s = 5 \times 10^{-4}$, a frequency $\Omega/2\pi = 20$ GHz and a spatial period $2\pi/|q| = 0.886$ μm. (All these parameters should be achievable in experiments.) The modulation is applied to half of the waveguide width so that the even and odd modes can couple efficiently. The modulation length L is chosen as the coherence length $l_{c0} = 2.19$ mm (Fig. 13.1b) for operation frequency ω_0 at 1.55 μm wavelength. Figure 13.4a shows the transmission for forward and backward directions. The bandwidth is 5 nm with contrast ratio above 30 dB.

For the loss induced by refractive index modulation schemes, e.g., carrier injection modulation, the contrast ratio remains approximately the same as the lossless case, since the modulation loss applies to transmission in both directions. Thus the isolation effect is not affected. As an example, the modulation strength used here $\delta/\varepsilon_s = 5 \times 10^{-4}$ results in a propagating loss of 1.5 cm^{-1} in silicon [14]. This causes an insertion loss about -3.5 dB while the bandwidth remains approximately unchanged (Fig. 13.4b).

In general, nonreciprocal effects can also be observed in intraband transitions involving two photonic states in the same photonic band. However, since typically $\Omega \ll \omega_1$, and the dispersion relation of a single band can typically be approximated as linear in the vicinity of ω_1, cascaded process [2], which generates frequencies at $\omega_1 + n\Omega$ with $n > 1$, is unavoidable, and it complicates the device performance. In contrast, the interband transition here eliminates the cascaded processes.

We would like to emphasize that the modulation frequency can be far smaller than the bandwidth of the signal. This is in fact one of the key advantages of using interband transition. The transition occurs from a fundamental even mode to a second-order odd mode. The generated odd mode can be removed with the use of mode filters that operate based on modal profiles. Examples of such mode filters can be found in [15, 16]. It is important to point out that such mode filters are purely passive and reciprocal, and can be readily implemented on chip in a very compact fashion. Moreover, later in this section, we discuss an implementation of an isolator without the use of modal filters.

13.3.1 Detailed Analysis of the Isolator Performance

Below in this section, based on the coupled mode theory, we analyze in details various aspects regarding the performance of the proposed isolator including in particular its operational bandwidth and device size.

13.3.1.1 Bandwidth

The dynamic isolator structure creates contrast between forward and backward propagations by achieving complete frequency conversion only in the forward direction. As discussed above, the modulation is chosen such that, it induces a phase-matched transition from an even mode at the frequency ω_0 to an odd mode at the frequency of $\omega_0 + \Omega$. The length of the waveguide is chosen to be the coherence length $l_c(\omega_0)$ for this transition, such that complete conversion occurs at this frequency ω_0 for the incident light. In order to achieve a broad band operation, one would need to achieve near-complete conversion for all incident light having frequencies ω in the vicinity of ω_0 as well. From (13.6), broad band operation therefore requires that

$$\Delta k(\omega) = 0$$
$$l_c(\omega) = L = l_c(\omega_0). \tag{13.7}$$

The first condition in (13.7) implies that the phase-matching condition needs to be achieved over a broad range of frequencies, and the second condition implies that the coherence length should not vary as a function of frequency. Deviations from these conditions result in a finite operational bandwidth.

Fig. 13.5 Forward
transmission as a function of
(**a**) phase mismatch and (**b**)
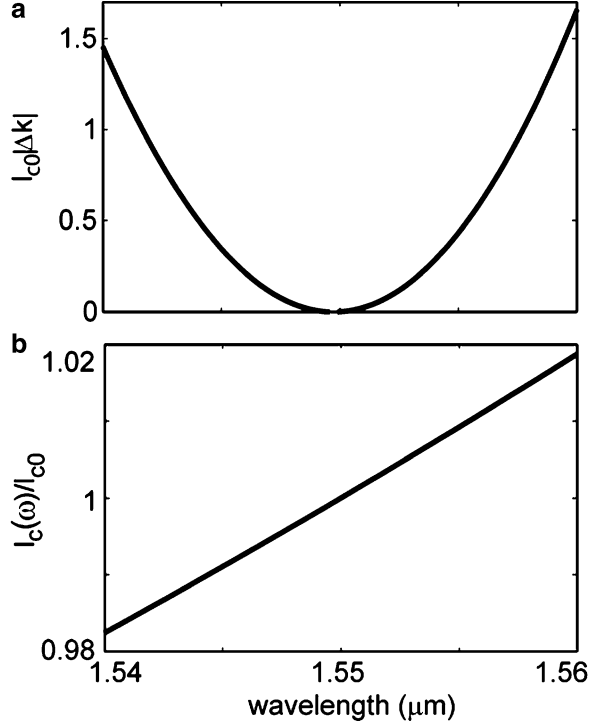coherence length variation
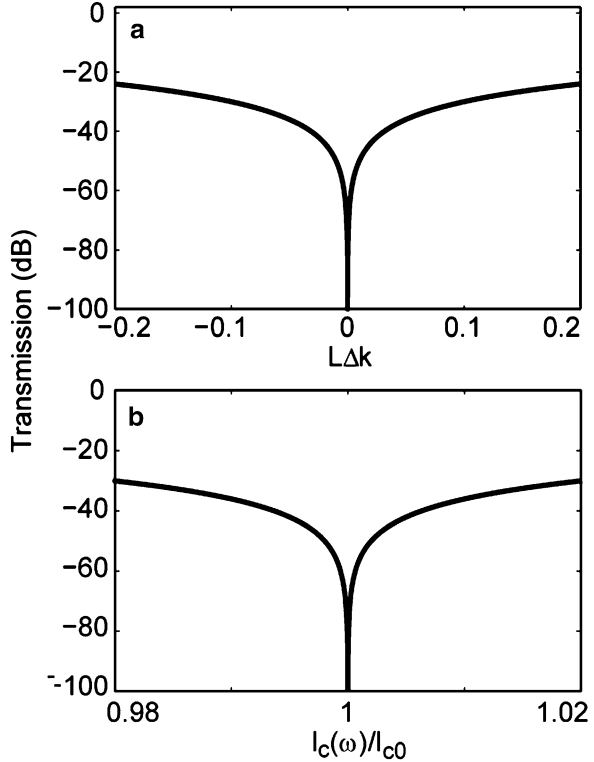
We consider the phase-matching condition first. In the vicinity of the design frequency ω_0, the wavevector mismatch can be approximated by $\Delta k = k_1(\omega) - k_2(\omega + \Omega) - q \approx ((1/v_{g1}(\omega)) - (1/v_{g2}(\omega + \Omega)))\Delta\omega + 1/2((d^2k_1(\omega)/d\omega^2) - (d^2k_2\omega + \Omega)/d\omega^2)\Delta\omega^2||_{\omega=\omega_0}$.

Thus, to minimize the phase mismatch, it is necessary, first of all, that the two bands have the same group velocities, i.e., the two bands are parallel to each other. Moreover, it is desirable that the group velocity dispersion of the two bands matches with one another. As a quantitative estimate, assuming that $l_c(\omega) \approx L$ for all frequencies, Fig. 13.5a shows the forward transmission as a function of $L\Delta k$. For a transmission below -30 dB, this requires a phase mismatch of $L\Delta k < 0.1$. As a concrete example for comparison purposes, Fig. 13.6a shows the phase mismatch $L\Delta k$ as a function of wavelength for the structure simulated in Fig. 13.4. Notice that $L\Delta k < 0.1$ over a bandwidth of 5 nm due to the mismatch of group velocity dispersion in the two guided mode bands. Thus the operating bandwidth of this device for 30 dB contrast is on the order of 5 nm.

For the second condition in (13.7), we note that in most waveguide structures, since the coherence length is determined by the modal profile, it generally varies slowly as a function of frequency. For example, for a waveguide with parameters chosen in Sect. 13.2, the coherence length varies $<2\%$ over 20 nm bandwidth

Fig. 13.6 Phase mismatch (**a**) and coherence length (**b**) as a function of wavelength for the device simulated in Fig. 13.4

around 1.55 μm wavelength (Fig. 13.6b). As a simple estimate of how coherence length variation impacts device performance, assuming that $\Delta k(\omega) = 0$ over a broad frequency range, we calculate the forward transmission as a function of coherence length given the modulation length $L = l_c(\omega = \omega_0)$ (Fig. 13.5b). For 2% variation of the coherence length, the forward transmission remains below -30 dB. Comparing Fig. 13.6a, b, therefore, we conclude that for the structure simulated in Fig. 13.4, the 5-nm bandwidth is primarily limited by group velocity dispersion of the two waveguide bands. Since the structure used in Fig. 13.4 is a rather simple, we believe that substantial further enhancement of operating bandwidth is achievable by optimization of waveguide geometry.

13.3.1.2   Device Size

The size of the isolator is determined by the coherence length l_c. Starting from (13.5), and taking into account the normalization of E field (13.3), the coherence length can be written as

$$l_c = \frac{4\pi}{\varepsilon_0 \int\limits_{-\infty}^{\infty} \delta(x)E_1(x)E_2(x)\mathrm{d}x} = \frac{2\pi}{\gamma}\sqrt{\frac{v_{g1}v_{g2}}{\omega_1\omega_2}} \approx \lambda_0 \cdot \frac{1}{\gamma} \cdot \frac{v_g}{c}, \qquad (13.8)$$

where $\gamma = (\int_{-\infty}^{\infty} \delta(x)E_1(x)E_2(x)dx)/(\sqrt{\int_{-\infty}^{\infty} \varepsilon(x)|E_1|^2 dx \int_{-\infty}^{\infty} \varepsilon(x)|E_2|^2 dx})$ characterizes the effect of modulation. In deriving (13.8), we assume that $\omega_1 \approx \omega_2 \equiv 2\pi c/\lambda_0$, where λ_0 is the wavelength in vacuum, since the modulation frequency is typically far smaller than the optical frequency. Moreover, the two bands are assumed to be parallel to each other, i.e., $v_{g1} \approx v_{g2} \equiv v_g$. Equation (13.8) indicates that the device size is proportional to the group velocity and is inversely proportional to the modulation strength. For a rough estimate, with a modulation strength $\gamma \sim (\delta/\varepsilon) \sim 10^{-4}$, operating at a wavelength of $\lambda \sim 1.5 \ \mu m$ and $v_g \approx c/3$, the coherence length $l_c \sim 5 \ mm$. To reduce the size, one can use stronger modulation strength and/or slow light waveguides.

13.3.1.3 Near-Phase-Matched Transition in the Backward Direction

In general, due to energy conservation constraint, a mode with a frequency of ω_1 can only make a transition to modes at $\omega_1 \pm \Omega$. In our design, the modulation is chosen to create a phase-matched transition in the forward direction. However, for most electro-optic or acoustic-optic modulation schemes, the modulation frequency $\Omega \leqslant 100 \ GHz$ is much smaller than the optical frequency. Consequently, as can be seen from Fig. 13.7a, in the backward direction the transition to the mode in the second band with a frequency $\omega_3 = \omega_1 - \Omega$ becomes nearly phase-matched. The wavevector mismatch of this transition is:

$$\Delta k_b = -k_2(\omega_1 - \Omega) + k_1(\omega_1) + q \approx \frac{2\Omega}{v_g}. \qquad (13.9)$$

Such a transition results in loss in the backward direction and thus a reduction of contrast between the forward and backward directions.

To calculate such transmission loss in the backward direction, we replace Δk in (13.6) with Δk_b. In general, in order to suppress such backward transmission loss, one needs to have:

$$\Delta k_b \cdot L \geq 1. \qquad (13.10)$$

Combining with (13.8), the condition of (13.10) is then transformed to:

$$\frac{2\lambda_0}{c} \cdot \frac{\Omega}{\gamma} \geq 1. \qquad (13.11)$$

Remarkably, we note from (13.11) that for electro-optic or acoustic-optic modulation schemes, the effects of weak refractive index modulation γ and low modulation frequency Ω cancel each other out. The use of weak refractive index modulation results in a long coherence length, which helps in suppressing the transition processes that are not phase matched. And it is precisely such a cancellation that enables the construction of dynamic isolators with practical modulation mechanisms.
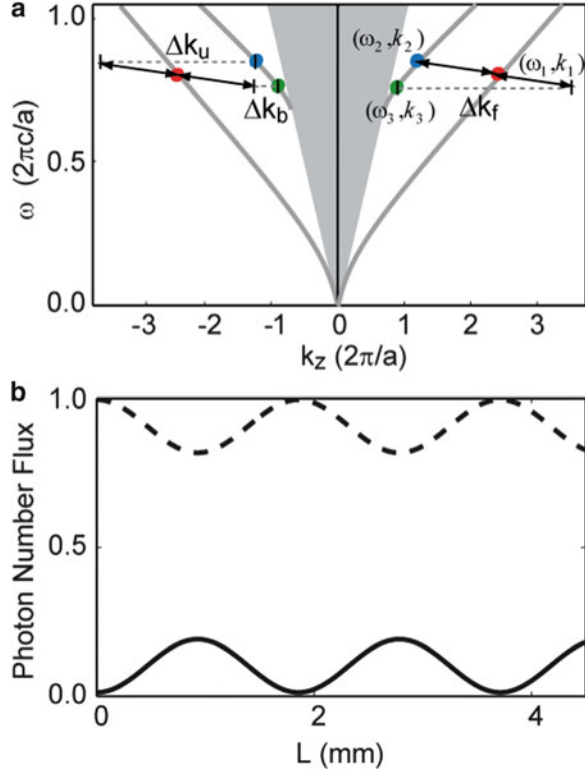
For the example shown in Fig. 13.4, the near-phase-matched transition in the backward direction has a $\Delta k_b = 2\pi/2.06$ mm and thus $\Delta k_b L = 6.7$, which results in a loss of -0.22 dB for the backward transmission (Fig. 13.7b).

13.3.2   Design Flexibility

In the previous sections, we have shown that by using interband transition, one can create nonreciprocal mode conversion in a waveguide. Such a waveguide works as an isolator when combined with a modal filter. The performance of such device can be analyzed and optimized using coupled mode theory. In this section, we present two examples to show that such nonreciprocal photon transition can be exploited in a wide range of structures to form nonreciprocal optical devices that satisfy diverse performance requirements. In the first example, we design a four-port isolator/circulator using nonreciprocal phase shift in the interband transitions. In the second example, we use a nonreciprocal ring resonator to demonstrate a compact design for optical isolation.
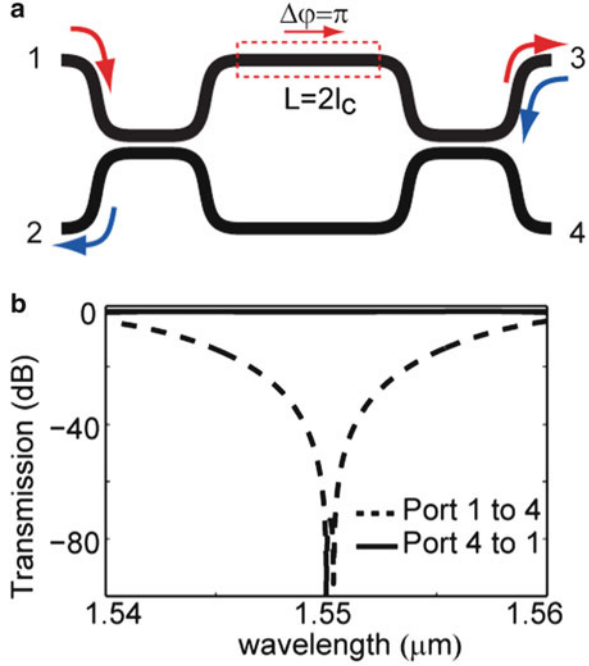
13.3.2.1 Four-Port Circulator

Figure 13.8a shows the design of a four-port circulator [13]. The structure consists
of a Mach–Zehdner interferometer, in which one waveguide arm is subject to the
dynamic modulation described above. In contrast to the design in Sect. 13.3,
however, here the length of the modulation region is chosen to be twice the
coherence length $L = 2l_c$. Thus, light passing through the modulated waveguide
in the forward direction will return to the incident frequency (Fig. 13.2a). However,
such light experiences a nonreciprocal phase shift due to the photonic transition
effect. The use of a Mach–Zehnder interferometer configuration then allows one to
construct a circulator. Here no filter is required, which significantly reduces the
device complexity.

   For concreteness, we assume that the interferometer has two arms with equal
length, and uses two 50/50 waveguide couplers. For such an interferometer, the
transmission is described by

$$\begin{pmatrix} b_u \\ b_l \end{pmatrix}_{\text{OUT}} = \frac{1}{2}\begin{pmatrix} 1 & i \\ i & 1 \end{pmatrix}\begin{pmatrix} T\exp(i\varphi_p) & 0 \\ 0 & \exp(i\varphi_p) \end{pmatrix}\begin{pmatrix} 1 & i \\ i & 1 \end{pmatrix}\begin{pmatrix} b_u \\ b_l \end{pmatrix}_{\text{IN}}. \quad (13.12)$$

Here, the sub-script "IN" and "OUT" label the input or output. $b_{u/l}$ are the input or
output amplitudes in the upper/lower arm. φ_p is the phase acquired due to propaga-
tion in the absence of modulation.

In (13.12), the transmission coefficient through the upper arm has an addition contribution from the photon transition:

$$T = e^{-iz\Delta k/2} \left[\cos\left(\frac{z}{2l_c} \sqrt{\pi^2 + (l_c\Delta k)^2} \right) + i \frac{l_c\Delta k}{\sqrt{\pi^2 + (l_c\Delta k)^2}} \sin\left(\frac{z}{2l_c} \sqrt{\pi^2 + (l_c\Delta k)^2} \right) \right],$$

(13.13)

which influences both the transmission amplitude and the phase as the wave passes through the upper arm. In our design, we assume a phase-matching modulation with $\Delta k = 0$ for the forward direction, and use a modulated region with $L = 2l_c$. Equation (13.13) shows $T = -1$. In contrast, for the light in the backward direction in the upper arm, in general the phase matching condition is not satisfied. Hence, $T \approx 1$. Thus, in this design, the modulation does not create any frequency conversion. Instead its sole effect is to induce a nonreciprocal phase shift in the upper arm.

The interferometer in Fig. 13.8 exploits such nonreciprocal phase to create a circulator. We have used the coupled mode theory developed in Sect. 13.3, to simulate this structure, assuming the same waveguide parameters as in Fig. 13.4. The results, shown in Fig. 13.8, indicate that lights injected into port 1 completely output through port 3, while in the time reversed case, lights injected into port 3 ends up in port 2. Therefore, this device has exactly the same response function of a four-port circulator. Unlike conventional design, however, no magnetic components are used inside the structure. Alternatively, the device can also function as a two-port isolator. Figure 13.8b shows the transmission spectra in both directions between ports 1 and 4: lights incident from port 4 transmit to port 1 while the reverse transmission is completely suppressed. The contrast ratio for the two directions is above 30 dB for a bandwidth of 5 nm (Fig. 13.8b).

13.3.2.2   Nonreciprocal Ring Resonator

As discussed before, the device size is determined by the coherence length, which typically is above millimeters unless slow light waveguides are used. Substantial reduction of the device footprint can be accomplished using resonator structure at the expense of a smaller operating bandwidth [3]. As an example, we consider a ring resonator (Fig. 13.9a) that supports two anticlockwise rotating resonances, at frequencies ω_1 and ω_2, respectively. Each resonance is further characterized by its wavevector k_1 and k_2 in the waveguide that forms the ring. These two resonances are coupled by applying a dielectric constant modulation along the ring with a profile $\delta(x) \cos[(\omega_1 - \omega_2)t - (k_1 - k_2)z]$, where z measures the propagation distance on the circumference of the ring in counterclockwise direction.

Fig. 13.9 (**a**) Schematic of
ring resonator designed for
nonreciprocal frequency
conversion. The *dark regions*
are modulated. (**b**) Schematic
of the modes in the ring-
waveguide coupling region
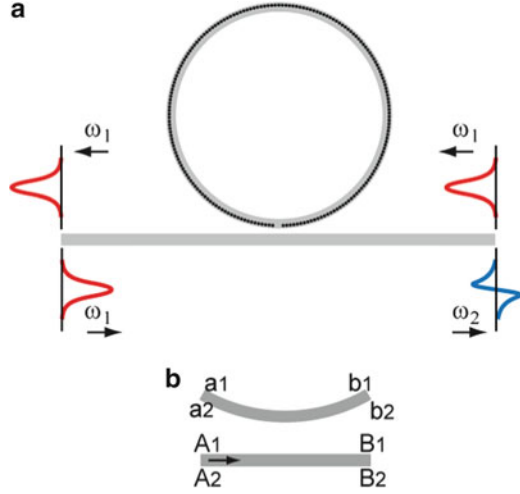
To describe the action of this structure, we note that upon completing one round
trip, the circulating amplitudes $a_{1,2}$ and $b_{1,2}$ of these two modes (Fig. 13.9b) are
related by:

$$\begin{pmatrix} a_1 \\ a_2 \end{pmatrix} = \begin{pmatrix} T_{11} & T_{12} \\ T_{21} & T_{22} \end{pmatrix} \begin{pmatrix} b_1 \\ b_2 \end{pmatrix}, \tag{13.14}$$

where the matrix elements are related to the transition amplitudes for a single round
trip, and can be calculated using (13.4). Each of these modes is also coupled to an
external waveguide as described by:

$$\begin{pmatrix} b_1 \\ B_1 \\ b_2 \\ B_2 \end{pmatrix} = \begin{pmatrix} r_1 & jt_1 & 0 & 0 \\ jt_1 & r_1 & 0 & 0 \\ 0 & 0 & r_2 & jt_2 \\ 0 & 0 & jt_2 & r_2 \end{pmatrix} \begin{pmatrix} a_1 \\ A_1 \\ a_2 \\ A_2 \end{pmatrix}. \tag{13.15}$$

The external waveguide is also assumed to support two modes with opposite
symmetry at the frequencies ω_1, ω_2 respectively. Here, the subscripts label the
two frequencies. $A_{1,2}$ and $a_{1,2}$ ($B_{1,2}$ and $b_{1,2}$) are the photon flux amplitudes in
the external and ring waveguides before (after) the coupler. The coefficients r, t are
taken to be real [17] and $r_{1,2}^2 + t_{1,2}^2 = 1$.

With incident light in mode 1 (i.e., $A_1 = 1$, $A_2 = 0$) of the external waveguide,
combining (13.14) and (13.15), we have

$$B_1 = \frac{r_1 - T_{11} - r_1 r_2 T_{22} + r_2 Det[T]}{1 - r_1 T_{11} - r_2 T_{22} + r_1 r_2 Det[T]}, \tag{13.16}$$

Fig. 13.10 Transmission spectra of a ring-resonator isolator. ω_0 corresponds to 1.55 μm wavelength. The waveguide-ring transmit coefficient is assumed to be $r_{1,2} = 0.95$
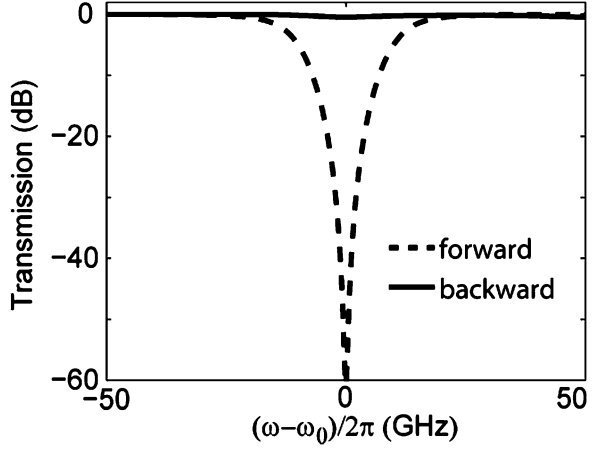
where *Det* stands for determinant. Thus, the condition for complete frequency conversion (i.e., $B_1 = 0$) is

$$r_1 - T_{11} - r_1 r_2 T_{22} + r_2 Det[T] = 0. \tag{13.17}$$

In the case that ring is lossless, $Det[T] = 1$ and $T_{11} = T_{22} = \cos((\pi/2)(L/l_c))$, where l_c is the coherence length and L is circumference of the ring. Complete conversion between the two modes can be achieved when the length of the ring is chosen to be

$$\cos\left(\frac{\pi}{2}\frac{L}{l_c}\right) = \frac{r_1 + r_2}{1 + r_1 r_2}. \tag{13.18}$$

With $r_{1,2} \to 1$, $L/l_c \to 0$, the device therefore can provide complete frequency conversion even when its length is far smaller than the coherence length.

As an example, now we use the same waveguide discussed in Fig. 13.4 to form a ring with a radius $r = 12.3$ μm. Such a ring supports two resonant modes: a first band resonant mode at 1.55 μm and a second band mode that is 50 GHz higher in frequency. (This is always achievable by fine tuning the radius and width of the waveguide.) A phase matching modulation is applied to the ring with a coherence length $l_c = 2.37$ mm. At the design wavelength 1.55 μm, the forward transmission is completed suppressed (Fig. 13.10). Here, the complete isolation is achieved with a device size much smaller than the coherence length.

In this section, we have provided some of detailed theoretical considerations for the dynamic isolator structures that we have recently proposed. In contrast to previously considered isolators based on material nonlinearity [9, 10] where isolation is only achievable for a range of incident power, the photonic transition effect studied here is *linear* with respect to the incident light: the effect does not depend upon the amplitude and phase of the incident light. Having a linear process is crucial because the device operation needs to be independent of the format, the

timing and the intensity of the pulses used in the system. In conclusion, the structure proposed here shows that on-chip isolation can be accomplished with dynamic modulation, in standard material systems that are widely used for integrated optoelectronic applications.

13.4   Photonic Transition for Tunable Resonance

In this section, we review the tunable resonance based on photonic transition. Resonance appears when a localized state couples to a continuum. In photonics, of particular interest is when the localized state is supported by an optical microcavity, and the continuum is one-dimensional such as in a waveguide. Such waveguide-cavity configurations find applications in filters, sensors, switches, slow-light structures, and quantum information processing devices.

In all applications of resonance, it is essential to accurately control its spectral properties. For the waveguide-cavity resonances, some of the important spectral properties are the resonance frequency, and the *external linewidth* due to waveguide-cavity coupling. The inverse of such linewidth defines the corresponding quality factor (Q) of the cavity.

In this part, we show that a single high-Q resonance can be created by dynamically inducing a photonic transition between a localized state and a one-dimensional continuum. Since the coupling between the continuum and the localized state occurs *solely* through dynamic modulations, both the frequency and the external linewidth of a single resonance are specified by the dynamics, allowing complete control of its spectral properties.

We start by first briefly reviewing the Anderson–Fano model [18, 19], which describes the standard waveguide-cavity systems:

$$H = \omega_c c^+ c + \int \omega_k a_k^+ a_k \mathrm{d}k + V \int (c^+ a_k + a_k^+ c)\mathrm{d}k. \qquad (13.19)$$

Here, ω_c is the frequency of a localized state that is embedded inside a one-dimensional continuum of states (Fig. 13.11a) defined by ω_k. c^+ (c) and a_k^+ (a_k) are the bosonic creation (annihilation) operators for localized and continuum states, respectively. V describes the interaction between them. Such a model supports a resonance at $\omega_0 = \omega_c$, with an external linewidth $\gamma = 2\pi(V^2/v_g)$ (defined as the full width at half maximum of the resonance peak). Here, $v_g \equiv \left.\frac{\mathrm{d}\omega_k}{\mathrm{d}k}\right|_{\omega_0}$.

In contrast to the standard Fano-Anderson model, our mechanism is described by the Hamiltonian: (Fig. 13.11b)

$$H = \omega_c c^+ c + \int \omega_k a_k^+ a_k \mathrm{d}k + (V + V_D \cos(\Omega t)) \int (c^+ a_k + a_k^+ c)\mathrm{d}k. \qquad (13.20)$$
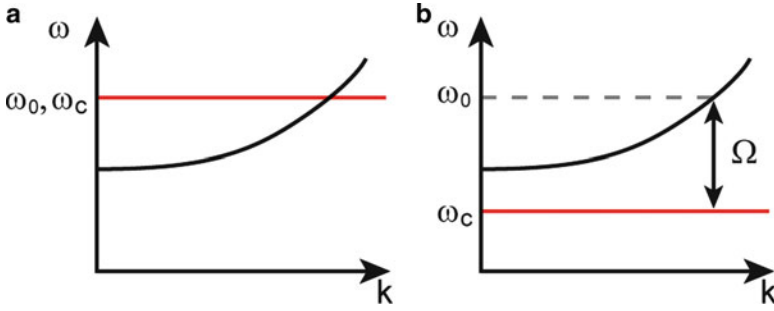
Fig. 13.11 Two different coupling mechanisms between a localized state and a one-dimensional continuum. (**a**) Static case: The frequency ω_c of the localized state lies in the band of the continuum. The static coupling between them results in a resonance at $\omega_0 = \omega_c$. (**b**) Dynamic case: The localized state has its frequency ω_c that falls outside the continuum. A modulation at a frequency Ω creates a photonic transition that couples them, resulting in a resonance at $\omega_0 = \omega_c + \Omega$

Here, unlike in (13.19), we assume that $\omega_k > \omega_c$ for any k. Consequently, the static coupling term $V \int (c^+ a_k + a_k^+ c) dk$ no longer contributes to the decay of the resonance. Instead, it only results in a renormalization of ω_c. The localized state decays *solely* through the dynamic term $V_D \cos(\Omega t) \int (c^+ a_k + a_k^+ c) dk$, which arises from modulating the system. Such modulation induces a photonic transition between the localized state and the continuum.

For the Hamiltonian of (13.20), one can derive an input–output formalism [20] in the Heisenberg picture, relating $C(t) = c(t)e^{-i\Omega t}$ to the input field operator $a_{\mathrm{IN}}(t)$ as:

$$\frac{\mathrm{d}}{\mathrm{d}t} C = -i(\omega_c + \Omega)C - \frac{\gamma}{2}C + i\sqrt{\gamma}a_{\mathrm{IN}}, \tag{13.21}$$

where $\gamma = 2\pi(((V_D/2)^2)/v_g)$ with $v_g = \left.\frac{\mathrm{d}\omega_k}{\mathrm{d}k}\right|_{\omega=\omega_c+\Omega}$. For an incident wave a_{IN} in the waveguide, the modulated system therefore creates a single resonance at the frequency $\omega_0 = \omega_c + \Omega$. Importantly, unlike the static system in (13.19), here both the frequency ω_0 and the external linewidth γ of the resonance are controlled by the dynamic modulation.

We now realize the Hamiltonian in (13.20) in a photonic crystal heterostructure [21] (Fig. 13.12a). The structure consists of a well and two barrier regions, defined in a line-defect waveguide in a semiconductor ($\varepsilon = 12.25$) two-dimensional photonic crystal. In the barrier regions, the crystal has a triangular lattice of air holes with a radius $r = 0.3a$, where a is the lattice constant. The waveguide supports two TE (H_z, E_x, E_y) modes with even and odd modal symmetry (Fig. 13.12c, light gray lines). In the well region, the hole spacing a' along the waveguide is increased to $1.1a$, which shifts the frequencies of the modes downward (Fig. 13.12c, dark lines) compared to those of the barriers. As a result, the odd modes in the well and the barriers do not overlap in frequencies. Thus, the well can support localized states, which are essentially standing waves formed by two
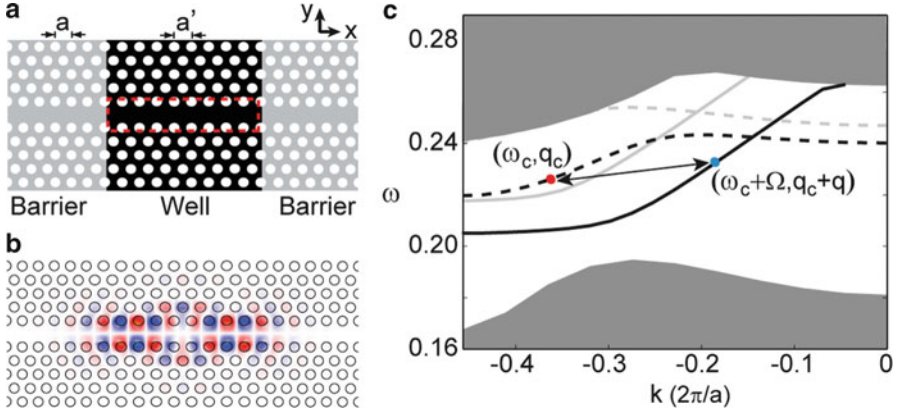
Fig. 13.12 (**a**) A photonic crystal heterostructure. The width of the waveguide measured from the centers of the holes on the two sides is $1.33a$. The *highlighted rectangle* represents the modulated region, which has dimensions of $2a \times 9.7a$. (**b**) Electric field (E_y) profile of a localized state in the well. *Red* and *blue* represent positive and negative maximum amplitudes. (**c**) Dispersion relation of the photonic crystal waveguide modes. The *dark* and *light gray lines* are for modes in the well and barriers, respectively. *Solid (dashed) lines* represent modes with even (odd) modal symmetry. *Shadowed regions* are the extended modes of the crystal region of the well

counter-propagating odd modes in the well. Figure 13.12b shows one such localized state at the frequency $\omega_c = 0.2252(2\pi c/a)$, with its corresponding waveguide mode at the wavevector $q_c = -0.37(2\pi/a)$ indicated by a red dot in Fig. 13.12c. Without modulation such a localized state cannot leak into the barrier and hence cannot be excited by wave coming from the barrier.

To induce a photonic transition, we modulate the dielectric constant of the well in the form of $\varepsilon_D = \Delta\varepsilon(y)\cos(\Omega t - qx)$. Here, the modulation frequency Ω is chosen such that an even mode in the well at the frequency $\omega_c + \Omega$ can leak into the barriers. The modulation wavevector q is selected to ensure a phase-matched transition between this even mode and the odd mode at (ω_c, q_c) that forms the localized state. Since these two modes have different symmetry, the modulation has an odd transverse profile: $\Delta\varepsilon(y) = \text{sign}(y)\Delta\varepsilon$, with $y = 0$ located at the waveguide center.

In the presence of the modulation, we consider an even mode incident from the left barrier, with a frequency ω in the vicinity of $\omega_c + \Omega$. As it turns out, for the even modes, the transmission coefficients into and out of the well are near unity. Thus, inside the well, the amplitudes of the even mode (Fig. 13.13, blue arrow) at the two edges, $A_{x=0}$ and $A_{x=L}$, are the input and output amplitudes of the system. As the even mode propagates forward from $x = 0$ to $x = L$, the modulation induces a transition to a copropagating odd mode at $\omega - \Omega$ (Fig. 13.13, red arrow). This transition process is described by [3]:

$$
\begin{pmatrix} A_{x=L} \\ B_{x=L} \end{pmatrix} = \begin{pmatrix} \exp(iLq_\omega) & 0 \\ 0 & \exp(iLq_{\omega-\Omega}) \end{pmatrix} \begin{pmatrix} \sqrt{1-\eta^2} & i\eta \\ i\eta & \sqrt{1-\eta^2} \end{pmatrix} \begin{pmatrix} A_{x=0} \\ B_{x=0} \end{pmatrix},
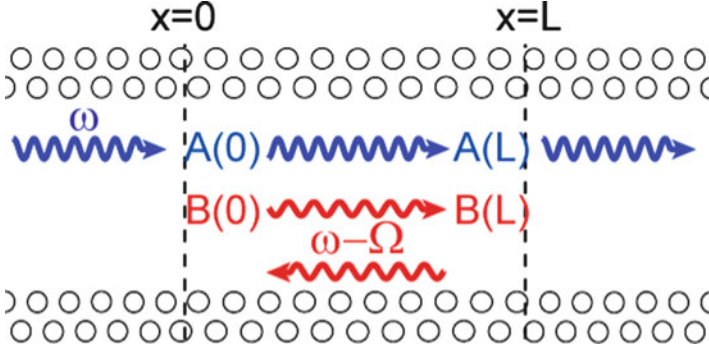$$

$$(13.22)$$

Fig. 13.13 The microscopic theory for photonic transition in the photonic crystal heterostructure. Incident light from the barrier at a frequency ω, as represented by the *blue arrows*, couples to a mode of the well at the frequency $\omega - \Omega$, as represented by the *red arrows*. The *dashed lines* indicate the edges of the well

where $B_{x=0}$ and $B_{x=L}$ are the amplitudes of the copropagating odd mode at $\omega - \Omega$ at the two edges, q_ω and $q_{\omega-\Omega}$ are the wavevectors of the two modes. For weak modulation, the transition rate $\eta = (\Delta\varepsilon/\varepsilon)L\kappa \ll 1$, where κ is the overlap factor between the two modes and the modulation profile.

Once the fields reach $x = L$, the odd mode is completely reflected, and propagates back to $x = 0$. We note that no significant photon transition occurs in the backward propagation, since the modulation profile does not phase-match between $(\omega, -q_\omega)$ and $(\omega - \Omega, -q_{\omega-\Omega})$. Consequently,

$$B_{x=0} = \exp(iLq_{\omega-\Omega} + i2\phi)B_{x=L}, \tag{13.23}$$

where ϕ is the reflection phase at the well edge. Also, since there is a localized state at ω_c, the round trip phase at ω_c is $2(Lq_{\omega_c} + \phi) = 2\pi n$ where n is an integer. Therefore, the round trip phase for the odd mode at $\omega - \Omega \approx \omega_c$ can be approximated as

$$2(Lq_{\omega-\Omega} + \phi) \approx 2\pi n + (\omega - \Omega - \omega_c)\frac{2L}{v_{gc}}, \tag{13.24}$$

where $v_{gc} = \left.\frac{d\omega}{dk}\right|_{\omega=\omega_c}$. Combined (13.22)–(13.24), the transmission spectrum is:

$$T = \frac{A_{x=L}}{e^{iLq_\omega}A_{x=0}} = \frac{\sqrt{1-\eta^2} - e^{i(\omega-\omega_0)\frac{2L}{v_{gc}}}}{1 - e^{i(\omega-\omega_0)\frac{2L}{v_{gc}}}\sqrt{1-\eta^2}} \approx \frac{\omega - \omega_0 - i\frac{\gamma}{2}}{\omega - \omega_0 + i\frac{\gamma}{2}}, \tag{13.25}$$

where $\gamma = (\Delta\varepsilon/\varepsilon)^2(\kappa^2 L v_{gc}/2)$.

The detailed microscopic theory thus predicts all-pass filter response for this dynamic system consisting of a waveguide coupled to a standing-wave localized state. In contrast, in the static system, coupling of a waveguide to a standing-wave

localized state always produces either band-pass or band-reflection filters. Moreover, the resonant frequency

$$\omega_0 = \omega_c + \Omega \qquad (13.26)$$

and the quality factor

$$Q_e \equiv \frac{\omega_0}{\gamma} = \left(\frac{\varepsilon}{\Delta\varepsilon}\right)^2 \frac{2\omega_0}{\kappa^2 L v_{gc}} \qquad (13.27)$$

are completely controlled by the modulation, in agreement with the phenomenological model (13.21).

We numerically test the theory using finite-difference time-domain (FDTD) simulations. We simulate a well with a length of $9.9a$. Such a well supports the localized state shown in Fig. 13.12b. The length of the modulated region $L = 9.7a$ (Fig. 13.12a). We excite the even modes in the left barrier, with a Gaussian pulse centered at $0.235(2\pi c/a)$, and a width of $0.001(2\pi c/a)$. Without the modulation, the transmission coefficient (Fig. 13.14a) is near unity. With the modulation (with a strength $\Delta\varepsilon/\varepsilon = 1.63 \times 10^{-2}$, a frequency $\Omega = 9.8 \times 10^{-3}(2\pi c/a)$, and a wavevector $q = 0.196(2\pi/a)$), the transmission spectrum shows little change (Fig. 13.14b). However, the group delay now exhibits a resonant peak with a quality factor $Q_e = 1.09 \times 10^4$ (Fig. 13.14c, blue line). The structure indeed becomes a high-Q all-pass filter.

The properties of this resonance are controlled by the modulation. The resonant frequency changes linearly with respect to the modulation frequency, as predicted (Fig. 13.14e). (When varying the modulation frequency, we also change the modulation wavevector at the same time to satisfy the phase-matching condition.) The resonance frequency is largely independent of the modulation strength (Fig. 13.14e). The width of the resonance, and the peak delay, can be adjusted by changing the modulation strength (Fig. 13.14d). As a comparison between theory (13.27) and simulations, Fig. 13.14f plots the quality factor as a function of the modulation strength at the fixed modulation frequency $\Omega = 9.8 \times 10^{-3}(2\pi c/a)$. The simulation agrees excellently with the theory. The theory curve is generated with only one fitting parameter: the modal overlap factor $\kappa = 0.99a^{-1}$, which agrees well to a direct and separate calculation of the well waveguide by itself that yields $\kappa = 1.16a^{-1}$. The difference can be attributed to the finite-size effect of the well–barrier interfaces.

We now comment on some of the challenges in the practical implementations. For the simulated structure above, according to (13.27), a modulation strength of $\Delta\varepsilon/\varepsilon = 5 \times 10^{-3}$, which is achievable using carrier injection in semiconductors [14], results in an external quality factor of $Q_e = 1.1 \times 10^5$. In comparison, the radiation quality factors of photonic crystal heterostructure cavities exceeded 10^6 in experiments [22].
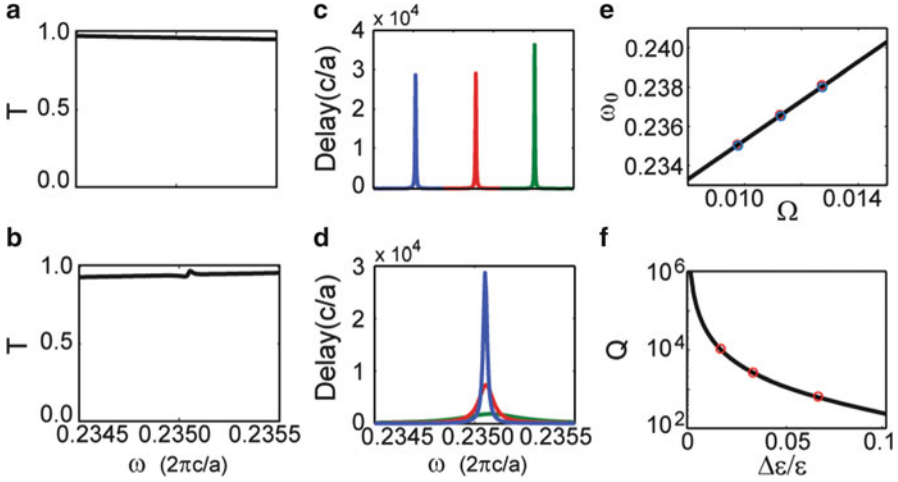
Fig. 13.14 Theory and simulation for the photonic transition process for the structure in Fig. 13.12. (**a**) Transmission spectrum for the unmodulated structure. (**b**) Transmission spectrum in the presence of modulation. The modulation has a frequency $\Omega = 9.8 \times 10^{-3}(2\pi c/a)$ and a strength of $\Delta\varepsilon/\varepsilon = 1.63 \times 10^{-2}$. (**c**) Group delay spectra, with $\Delta\varepsilon/\varepsilon$ fixed at 1.63×10^{-2}. The *blue, red* and *green lines* correspond to $\Omega = 9.8 \times 10^{-3}, 11.3 \times 10^{-3}$ and $12.8 \times 10^{-3}(2\pi c/a)$, respectively. (**d**) Group delay spectra, with Ω fixed at $9.8 \times 10^{-3}(2\pi c/a)$. The *blue, red*, and *green lines* correspond to $\Delta\varepsilon/\varepsilon = 1.63 \times 10^{-2}, 3.27 \times 10^{-2}$ and 6.53×10^{-2}. (**e**) Resonant frequency as a function of the modulation frequency. The *blue* and *red circles* corresponds to modulation strength of $\Delta\varepsilon/\varepsilon = 1.63 \times 10^{-2}$ and 3.27×10^{-2} respectively. *Circles* are simulation results as determined the peak location of group delay spectra, and the line is from analytical calcualtion. (**f**) Quality factor as a function of modulation strength. *Circles* are simulation results as determined from the peak width in (**d**), the line is from analytic calculation

Regarding the required modulation frequencies, in the simulation, $\Omega = 9.8 \times 10^{-3}(2\pi c/a)$ represents a modulation frequency of 8.1 THz, when the resonance frequency $\omega_0 = 0.235(2\pi c/a)$ corresponds to the wavelength of 1.55 μm. This is in principle achievable, since many index modulation scheme has intrinsic response time below 0.1 ps [23].

As final remarks, in our scheme, the tuning range for the resonant frequency is ultimately limited by the intrinsic response time of the material. Thus, the resonant frequency of the structure have a much wider tuning range, and can be reconfigured with a much higher speed, compared with conventional mechanisms. Moreover, the modulation frequency can typically be specified to a much higher accuracy [24], resulting in far more accurate control of the resonant frequency. Lastly, the localized state here is "dark" since it does not couple to the waveguide in the absence of modulation. Our scheme, which provides a dynamic access to such a dark state, is directly applicable for stopping and storage of light pulses, since the existence of a single dark state is sufficient [25].

13.5 Conclusion

In this chapter, we review the application of photonic transition for optical isolation and tunable resonance. These applications rely on photonic structures that can be dynamically modulated. Experimental techniques to achieve these dynamic structures have undergone fast development. One of the prominent techniques is to use carrier injection to modulate refractive index. Moreover, novel technique based on optical force has also emerged, such as the optomechanical modulation [26]. These developments open exciting opportunities for dynamic photonic structures.

References

1. J.N. Winn, S.H. Fan, J.D. Joannopoulos, E.P. Ippen, Phys. Rev. B **59**(3), 1551–1554 (1999)
2. P. Dong, S.F. Preble, J.T. Robinson, S. Manipatruni, M. Lipson, Phys. Rev. Lett. **100**(3), 033904 (2008)
3. Z. Yu, S. Fan, Nat. Photon. **3**(2), 91–94 (2009)
4. Z. Yu, S. Fan, Appl. Phys. Lett. **96**(1), 011108 (2010)
5. R.L. Espinola, T. Izuhara, M.C. Tsai, R.M. Osgood, Opt. Lett. **29**(9), 941–943 (2004)
6. M. Levy, J. Opt. Soc. Am. B: Opt. Phys. **22**(1), 254–260 (2005)
7. T.R. Zaman, X. Guo, R.J. Ram, Appl. Phys. Lett. **90**(2), 023514 (2007)
8. H. Dotsch, N. Bahlmann, O. Zhuromskyy, M. Hammer, L. Wilkens, R. Gerhardt, P. Hertel, A.F. Popkov, J. Opt. Soc. Am. B: Opt. Phys. **22**(1), 240–253 (2005)
9. M. Soljacic, C. Luo, J.D. Joannopoulos, S.H. Fan, Opt. Lett. **28**(8), 637–639 (2003)
10. K. Gallo, G. Assanto, K.R. Parameswaran, M.M. Fejer, Appl. Phys. Lett. **79**(3), 314–316 (2001)
11. S.K. Ibrahim, S. Bhandare, D. Sandel, H. Zhang, R. Noe, Electron. Lett. **40**(20), 1293–1294 (2004)
12. G. Shvets, Appl. Phys. Lett. **89**, 141127 (2006)
13. Z. Yu, S. Fan, Appl. Phys. Lett. **94**(17), 171116 (2009)
14. B.R. Bennett, R.A. Soref, J.A. Delalamo, IEEE J. Quant. Electron. **26**(1), 113–122 (1990)
15. Y. Jiao, S.H. Fan, D.A.B. Miller, Opt. Lett. **30**(2), 141–143 (2005)
16. B.T. Lee, S.Y. Shin, Opt. Lett. **28**(18), 1660–1662 (2003)
17. H.A. Haus, *Waves and Fields in Optoelectronics* (Prentice-Hall, Englewood Cliffs, NJ, 1984)
18. U. Fano, Phys. Rev. **124**(6), 1866–1878 (1961)
19. P.W. Anderson, Phys. Rev. **109**, 1492 (1958)
20. D.F. Walls, G.J. Milburn, *Quantum Optics* (Springer, Berlin, 1994)
21. B.S. Song, S. Noda, T. Asano, Y. Akahane, Nat. Mater. **4**(3), 207–210 (2005)
22. E. Kuramochi, M. Notomi, S. Mitsugi, A. Shinya, T. Tanabe, T. Watanabe, Appl. Phys. Lett. **88**(4), 041112 (2006)
23. S. Schmittrink, D.S. Chemla, W.H. Knox, D.A.B. Miller, Opt. Lett. **15**(1), 60–62 (1990)
24. T.W. Hansch, Rev. Mod. Phys. **78**(4), 1297 (2006)
25. C.R. Otey, M.L. Povinelli, S.H. Fan, J. Lightwave Technol. **26**(21–24), 3784–3793 (2008)
26. M. Eichenfield, J. Chan, R.M. Camacho, K.J. Vahala, O. Painter, Nature **462**, 78–82 (2009)